Plasticity and fracture behavior of Inconel 625 manufactured by laser powder bed fusion: comparison between as-built and stress relieved conditions

Shipin Qin[1], Theresa C. Novak[1], Madeline K Vailhe[1], Zi-Kui Liu[1], Allison M. Beese[1,2,*]

[1] Department of Materials Science and Engineering, The Pennsylvania State University, University Park, PA 16802, USA.

[2] Department of Mechanical Engineering, The Pennsylvania State University, University Park, PA 16802, USA.

[*] Corresponding author: amb961@psu.edu

Abstract

In this study, the influence of stress relief on the plasticity and fracture behavior of Inconel 625 fabricated through laser powder bed fusion additive manufacturing (AM) was investigated. The as-built versus stress relieved microstructures were compared, showing similar grain structures but the presence of ~10 vol. % δ phase in the stress relieved condition, and no δ phase in the as-built condition. Mechanical tests under plane strain tension were performed on the stress relieved samples, and an anisotropic plasticity model was calibrated and validated using finite element simulations. Uniaxial and notched tension tests were performed on both as-built and stress relieved samples to probe the effect of stress relief on stress state- and direction-dependent fracture behavior. It was found that on average, the fracture strain of the stress relieved samples along the build direction was 30% higher than that along the perpendicular build direction in the stress state range studied, and the stress relief heat treatment resulted in a

45% decrease in fracture strain. The fracture strain in stress relieved samples was more strongly dependent on stress state than in as-built samples.

Keywords: Laser powder bed fusion; Inconel 625; ductile fracture; stress state dependence

1. Introduction

Nickel-based superalloy Inconel 625 (IN625) is widely used in the aerospace industry for its high strength and excellent corrosion resistance at both room and elevated temperatures [1]. Due in part to its good weldability [1], it has been investigated as an alloy of interest for AM [2–5]. Due to complex thermal histories and constraints during fabrication, residual stresses are often present in additively manufactured materials, and stress relief post processing is thus commonly used [6].

The American Society for Metals (ASM international)-recommended process of stress relief for conventionally processed IN625 at 870 °C [7] is often performed for AM-processed IN625 [2,8]. In the as-built state, the typical microstructure of laser powder bed fusion (L-PBF) IN625 is of cellular dendrites with a primary dendrite spacing on the order of 1 μm [2,3]. Through energy dispersive X-ray spectroscopy (EDS) analysis, researchers have reported that the dendritic cores are enriched in Cr and Ni, while the inter-dendritic regions are enriched in Nb and Mo with respect to the nominal alloy composition [2,8]. Both experimental observations [1,9–11] and computational studies [12] have revealed that at 870 °C, the δ phase is an

equilibrium phase in IN625, but in wrought IN625, the δ phase is rarely observed after one hour at 870 °C due to its slow transformation kinetics. On the other hand, the δ phase has been repeatedly observed in L-PBF IN625 after the same heat treatment [2,8,13,14]. A comparison of the time-temperature-transformation (TTT) diagrams for the δ phase in elementally homogenous wrought IN625 and in elementally heterogeneous L-PBF IN625 showed that the formation of 1 vol. % δ phase at 870 °C requires ~ 20 hours in the former but only ~ 0.3 hours in the latter [15,16]. Through solidification and precipitation simulations, Lindwall et al. [12] showed that this accelerated transformation kinetics of the δ phase in L-PBF IN625 was due to the variation in local chemical composition, namely high concentrations of Nb and Mo in interdendritic regions, resulting from solidification during the AM processes.

The presence of the brittle δ phase in IN625 strengthens the material but also decreases its ductility and corrosion resistance [3,15,17]. For example, Mu et al. heat treated cast alloy IN625 at 750 °C for different durations to get different amounts of δ phase, and performed uniaxial tension tests on the resultant materials [17]. Their measurements revealed that with increasing volume fraction of the δ phase, the ultimate tensile strength (UTS) of the material increased, and the elongation of the material decreased.

Prior studies have focused on uniaxial tension only, which is insufficient for a comprehensive understanding to the mechanical properties of L-PBF IN625 in applications in which materials may be subjected to multiaxial loading. The plasticity and fracture behavior of both conventionally processed metals [18–20] and additively manufactured metals [21–25] are stress state dependent. Therefore, the current study focuses on investigating the influence of stress relief on the multiaxial plasticity and fracture behavior of L-PBF IN625 through mechanical

testing, plasticity modeling, and finite element simulations of both as-built and stress relieved samples. The microstructures of both as-built and stress relieved L-PBF IN625 were characterized, showing no δ phase in the as-deposited condition, and the presence of δ phase after stress relief, consistent with observations reported in literature. The large deformation multiaxial plasticity behavior was characterized under uniaxial tension, notched tension, and plane strain tension. An anisotropic plasticity model was calibrated, which was able to capture the stress-state and direction-dependence of mechanical behavior seen in experiments. The stress state dependent fracture strain was obtained through a combined experimental-computational approach, and the influence of orientation, stress relief, and stress state on the fracture behavior was quantified.

2. Experiments

2.1. Material and microstructure characterization

IN625 walls were deposited onto a Toolox 33 steel baseplate using a 3D Systems ProX DMP 320 L-PBF system. Two builds were made: one used powder provided by Carpenter (Carpenter Powder Products, Corp.) and one used powder provided by 3D Systems. Both batches contained powder with diameters ranging from 15 to 45 μm. A laser power of 253 W, scan speed of 500 mm/s, hatch spacing of 0.1 mm, and layer thickness of 0.06 mm were used in fabrication of both builds. Rectangular walls measuring 14 mm × 65 mm × 65 mm were fabricated from which tensile specimens along the build direction (BD) and the perpendicular-build direction (PBD) were extracted, while walls measuring 30 mm × 70 mm × 55 mm were fabricated from which to

extract plasticity specimens along the BD. The build using Carpenter powder was fabricated to 46 mm tall due to material limitations, and the walls were removed from the baseplate in the as-built state. The build using 3D Systems powder was fabricated to 65 mm tall, and the walls were subjected to a stress relief heat treatment at 870 °C for 2 hours before removal from the baseplate. The elemental compositions of the as-built and stress relieved walls were analyzed (Luvak Inc., Boylson, MA) and are reported in **Table 1**. The carbon content was measured using combustion infrared detection, adhering to ASTM E1019-18, while the contents of other elements were measured using direct current plasma emission spectroscopy, adhering to ASTM E1097-12.

Samples were machined from both as-built and stress relieved walls, and mounted and polished using standard metallographic techniques with a final polish using 0.04 μm alumina suspension. The samples were then electrolytically etched using 10 wt. % oxalic acid at 4 V for 20 s. The surfaces of the etched samples were observed using a scanning electron microscope (SEM, FEI Apreo). On the same SEM instrument, the spatial variation of composition was analyzed using an EDS detector (Ultim Max, Oxford Instruments), and the grains were analyzed using an electron backscatter diffraction (EBSD) detector (Oxford Symmetry).

2.2. Mechanical tests

Uniaxial tension and notched tension specimens were extracted from both the as-built and stress relieved walls using wire electrical discharge machining (EDM). The uniaxial tension specimen geometry is shown in **Figure 1**a, which complies with ASTM E8 [26]. The notched

tension specimen geometries are shown in **Figure 1**b. Three different notch radii were studied: R = 2, 4, and 12 mm, resulting in different stress states at the specimen centers. For uniaxial and notched tension tests, specimens from the stress relieved walls were extracted with the tensile direction either along the PBD or the BD, while those from the as-built walls were extracted with the tensile direction along the PBD only due to limited material and build height. The orientations of the specimen are also illustrated in **Figure 1**c.

Multiaxial plasticity specimens, with the geometry shown in **Figure 1**d, were extracted from stress relieved walls using wire EDM. The vertical direction of the specimens (*y* in **Figure 1**d) was parallel to the BD, as illustrated in **Figure 1**c. The large aspect ratio in the gauge section of this specimen geometry prevents contraction in the horizontal direction (*x* in **Figure 1**d), ensuring that the gauge section width stays constant throughout deformation, which results in a plane strain condition (non-zero vertical and thickness strains, but zero strain in the horizontal direction). At the same time, its thin thickness also ensures a plane stress condition, with zero stress through the thickness. The specimen details are similar to those reported in ref. [27].

In all of the mechanical tests, digital image correlation (DIC) was used for surface deformation measurement. A uniform white basecoat followed by a random black speckle pattern was applied to the specimen surface before testing. During the tests, a digital camera (Point grey GRAS-50S5M-C) was used to take images of the specimen surface at a frequency of 1 Hz. The surface deformation was analyzed from the recorded images using VIC-2D (Correlated Solutions).

The uniaxial tension and notched tension specimens were tested on an electromechanical load frame (MTS Criterion Model 43) equipped with a 10 kN load cell. The uniaxial tension tests were performed under quasi-static loading with a loading strain rate on the order of 10^{-4} s^{-1}. In the DIC analysis, a 21mm-long vertical virtual extensometer was placed at the center of the specimen for displacement and strain calculations. The notched tension tests were loaded at a rate of 0.005 mm/s, and a virtual extensometer of 15 mm long was used to calculate displacements. The multiaxial plasticity tests were performed on a custom-made dual-actuator hydraulic test machine (MTS System Corp., see schematic in ref. [28]). The specimens were tested under displacement control with a vertical loading rate of 0.2 mm/min, with no horizontal displacement. A 3 mm tall virtual extensometer at the center of the specimen was used for strain measurement. All of the tests were performed twice to ensure repeatability of the results. In uniaxial tension, the relative error between the tests, calculated based on the engineering stress, was ~ 0.25% on the as-built samples and ~ 0.10% on the stress relieved samples. In notched tension, the relative error between the tests, calculated based on the force, was ~ 0.83% on the as-built samples and ~ 0.55% on the stress relieved samples. The relative error in plane strain tension tests was 1.12%.

3. Results and discussion

The microstructures of both the as-built and the stress relieved samples characterized by EBSD and SEM are shown in **Figure 2**. The EBSD images show that the grains in both samples were elongated along the build direction, as is typical for additively manufactured materials [8],

and the grain size did not show any significant difference between the as-built and the stress relieved samples. However, the SEM images reveal distinct microstructures between the as-built and stress relieved L-PBF IN625. The as-built sample exhibited a dendritic microstructure, with a primary dendritic spacing on the order of 1 μm, consistent with existing literature [2,3]. After stress relief heat treatment, plate-like precipitates were observed, which were rich in Nb and Mo and depleted of Cr, as shown by the EDS results in **Figure 3**. Literature data indicate that these precipitates are the δ phase (Ni_3Nb) [2,29]. As discussed by Lindwall et al. [12], the formation of the δ phase in L-PBF IN625 during stress relief is a result of elemental segregation caused by the rapid solidification during AM fabrication. To estimate the volume fraction of these precipitates, image analysis was performed by converting the SEM micrograph in **Figure 2**d to a binary image, and then calculating the ratio of number of white pixels to the total number of pixels. This calculation gave an approximate δ phase volume fraction of 10%.

3.1. Uniaxial tension results

Engineering stress versus strain curves obtained from uniaxial tension tests are shown in **Figure 4**. The engineering strains in the figure were obtained through virtual extensometers in the DIC analyses as described above. Due to the elongated grains along the build direction, the behavior of the stress relieved specimens was anisotropic, with a higher UTS (1128 MPa) and a lower elongation (24%) along the PBD compared to the that of specimens along the BD (1089 MPa and 34%). In addition, the PBD specimens from the as-built wall exhibited lower UTS (1035 MPa) and higher elongation (32%) compared to the PBD specimens from the stress relieved wall. Due to the similarity in grain size and morphology observed in **Figure 2**a and b,

this difference can be attributed to the presence of the δ phase in the stress relieved specimens. That is, the presence of ~10 vol. % δ phase increased the UTS of the samples by 9% and reduced the elongation under uniaxial tension by 27%.

The uniaxial tension properties of additively manufactured IN625, with and without heat treatment, have been extensively investigated [4,14,17,30,31]. The reported UTS versus ductility values for these studies are plotted in **Figure 5** with additional information summarized in **Table 2**. Compared to hot isostatic pressing (HIP), stress relief heat treatment has been shown to result in an increased UTS but decreased elongation for L-PBF IN625. The UTS and elongation values of the as-built specimens in the current study are comparable to those reported in the literature. However, the stress relieved samples in the present study had a higher UTS and a lower elongation compared to the other referenced stress relieved L-PBF IN625 alloys. This is due to the fact that in the present study, the samples were heat treated for 2 hrs at 870 °C, as recommended by the LPBF manufacturer (3D Systems) based on their process, compared to only 1 hr in the other studies referenced, resulting in a higher fraction of δ phase compared to those reported in the literature.

3.2. Plane strain tension results

As the experimental data under uniaxial tension indicate material anisotropy, an anisotropic plasticity model is required to capture the alloy's mechanical behavior. However, calibration of anisotropic plasticity models generally requires experimental data beyond that of just uniaxial tension in two directions. In addition, structural components are subjected to multiaxial loading

conditions in service, under which the mechanical behavior can be significantly different than under uniaxial loading conditions. Therefore, for adoption of L-PBF IN625 for structural components, it is critical to characterize its mechanical response under multiaxial loading conditions. In the present study, the stress relieved sample was tested under plane strain tension following the procedure detailed in Section 2.2, which provided information on this sample's performance under biaxial loading as well as the additional data required to calibrate the anisotropic plasticity model.

The experimental results are presented as the von Mises equivalent plastic strain, $\bar{\varepsilon}_{vM}^{p}$, versus the von Mises equivalent stress, $\bar{\sigma}_{vM}$, in **Figure 6**, with these measures defined as [32]:

$$\bar{\varepsilon}_{vM}^{p} = \int_{0}^{t} d\bar{\varepsilon}_{vM}^{p} = \int_{0}^{t} \sqrt{\frac{2}{3}\left[\left(d\varepsilon_{11}^{p}\right)^{2} + \left(d\varepsilon_{22}^{p}\right)^{2} + \left(d\varepsilon_{33}^{p}\right)^{2}\right] + \frac{4}{3}\left(d\varepsilon_{12}^{p}\right)^{2}} \qquad \text{Eq. 1}$$

$$\bar{\sigma}_{vM} = \sqrt{\sigma_{11}^{2} - \sigma_{11}\sigma_{22} + \sigma_{22}^{2} + 3\sigma_{12}^{2}} \qquad \text{Eq. 2}$$

where the subscript 1 refers to the material direction perpendicular to the build direction, and 2 refers to that parallel to the build direction. Note that due to plane stress approximation, $\sigma_{33} = 0$ was applied in the above definitions. The calculated $\bar{\varepsilon}_{vM}^{p}$ versus $\bar{\sigma}_{vM}$ curves for uniaxial tension and plane strain tension are compared with each other in **Figure 6**, which reveals that the strain hardening behavior of the material is not only anisotropic, but also stress state dependent.

3.3. Anisotropic plasticity modeling

To describe the anisotropic and stress state dependent plasticity behavior observed in experiments, the Hill48 plasticity model was adopted [33]. Similar to above, $\sigma_{33} = 0$ will be applied in the definitions below. The yield criterion of the Hill48 model is given as:

$$\Phi = \bar{\sigma}_{Hill48} - \sigma_y\left(\bar{\varepsilon}^p_{Hill48}\right) = 0 \qquad \text{Eq. 3}$$

where σ_y is the yield stress, the Hill48 equivalent stress, $\bar{\sigma}_{Hill48}$, is given as:

$$\bar{\sigma}_{Hill48} = \sqrt{P_{11}\sigma_{11}^2 - 2P_{12}\sigma_{11}\sigma_{22} + \sigma_{22}^2 + P_{33}\sigma_{12}^2}, \qquad \text{Eq. 4}$$

and $\bar{\varepsilon}^p_{Hill48}$ is the Hill48 equivalent plastic strain with its incremental form defined as:

$$d\bar{\varepsilon}^p_{Hill48} = \sqrt{\frac{\left(d\varepsilon^p_{11}\right)^2 + P_{11}\left(d\varepsilon^p_{22}\right)^2 - 2P_{12}d\varepsilon^p_{11}d\varepsilon^p_{22} + \frac{1}{P_{33}}\left(2d\varepsilon^p_{12}\right)^2}{P_{11} - P_{12}^2}} \qquad \text{Eq. 5}$$

P_{11}, P_{12}, and P_{33} in the above equations are model parameters that describe anisotropy and stress state dependence, and $\bar{\sigma}_{Hill48}$ and $\bar{\varepsilon}^p_{Hill48}$ are the variables used to describe the strain hardening behavior of the material.

The flow rule, which describes the evolution of the plastic strain components, is defined as:

$$\dot{\varepsilon}^p_{ij} = \dot{\gamma}\frac{\partial\Phi}{\partial\sigma_{ij}}, i = 1,2, j = 1,2 \qquad \text{Eq. 6}$$

where $\dot{\gamma}$ is the plastic multiplier.

The yield stress σ_y in Eq. 3 is a function of $\bar{\varepsilon}^p_{Hill48}$. In the present study, this strain hardening function is taken to be:

$$\dot{\sigma}_y = nA(\varepsilon_0 + \dot{\bar{\varepsilon}}^p)^{n-1} \text{ for } \bar{\varepsilon}^p \leq \bar{\varepsilon}^p_{necking}$$
$$\dot{\sigma}_y = K\dot{\bar{\varepsilon}}^p \text{ for } \bar{\varepsilon}^p > \bar{\varepsilon}^p_{necking} \quad \text{Eq. 7}$$

where A, ε_0, and n are the Swift law parameters [24], K is the slope of a linear extrapolation of strain hardening after necking, and $\bar{\varepsilon}^p_{necking}$ is the strain level when necking starts in uniaxial tension along the BD.

In the present study, the strain hardening parameters (A, ε_0, n, and K) were calibrated based on the uniaxial tension results along the BD for the stress relieved sample, and based on the uniaxial tension along the PBD for the as-built sample. Specifically, A, ε_0, and n were determined by direct fitting of the respective strain hardening curves before necking using the least squares method. The uniqueness of their values was ensured by minimizing the squared error between the equation and the experimental data points. The slope of linear extrapolation K, which cannot be determined directly due to localized necking, was determined iteratively through comparing finite element simulations using the uniaxial tension model described in Section 3.4 with experiments until the force-displacement behavior was captured, e.g., [34–36]. Two of the parameters describing anisotropy and stress state dependence, P_{11} and P_{12}, were calibrated based on the strain hardening rate in uniaxial tension along both orientations and in plane strain tension along the BD of the stress relieved sample. Since no shear test was performed, $P_{33} = 3$ was assumed, which is the value for an isotropic material. Ideally, P_{11}, P_{12}, and P_{33} would be calibrated separately for the as-built sample and the stress relieved sample; however, limited material precluded the collection of experiment data in plane strain tension for the as-built sample, so these parameters were assumed to be the same for both conditions of the L-PBF IN625. This assumption of similar anisotropy between the two conditions can be

partially validated by the similarity of the grain morphology in the two samples. The calibrated material model parameters are summarized in **Table 3**.

3.4. Validation of the plasticity model

The plasticity model above was implemented into finite element software ABAQUS [37] for model validation. For the uniaxial tension and notched tension specimens, one eighth of the specimen was modeled, and symmetric boundary conditions were applied along all three cut planes. An illustration of the applied boundary conditions is given in **Figure 7**. The uniaxial tension specimen was discretized with 9600 hexahedron elements (ABAQUS element type C3D8 [37]), with the smallest element size being 0.1 mm and located at the specimen center. The notched tension specimens were also discretized with hexahedron elements (ABAQUS element type C3D8 [37]), with the element size decreasing towards the specimen center. Through a mesh size study, it was found that regardless of the notch radius, when the mesh size at the specimen center was 0.1 mm or smaller, the local $\bar{\varepsilon}^{p}_{Hill48}$ value at the center (at the displacement to fracture) increased less than 1.5% when the element size was decreased by half. Therefore, a minimum element size of 0.1 mm was adopted for the notched tension specimens, which resulted in 840 elements for R=2 mm, 1004 elements for R=4 mm, and 884 elements for R=12 mm. An illustration of the notched tension specimen with R=2 mm being discretized with the converged mesh size is shown in **Figure 7**.

The simulated engineering stress versus strain curves for uniaxial tension are compared with experimental data in **Figure 8**. While an iterative process was used to adjust K so that the

uniaxial tension simulations along the PBD of the as-built sample and along the BD of the stress relieved sample matched their respective experiments, the good agreement before the maximum stress of these curves, as well as for uniaxial tension along the PBD of the stress relieved sample, show that the calibrated model was able to capture the mechanical anisotropy of the material.

The notched tension simulation results are compared with experimental data in **Figure 9**, showing that the simulations were able to capture the anisotropic mechanical behavior of stress relieved L-PBF IN625, as well as the mechanical behavior of L-PBF IN625 before and after stress relief heat treatment. The good agreement between simulations and experiments support the adoption of the Hill48 plasticity model and the assumption that the as-built sample and the stress relieved sample share the same P_{11}, P_{12}, and P_{33} values. Note that the displacement data in the notched tension tests were obtained from a 15 mm-long virtual extensometer in the DIC analysis.

3.5. Fracture behavior

Despite the abundance of experimental data under uniaxial tension, as shown in **Table 1** and **Figure 5**, and the understanding that the presence of the δ phase limits the uniaxial tension ductility of L-PBF IN625, a study quantifying the effect of stress state on the ductility of L-PBF IN625 without and with the δ phase is absent. The notched tension experiments and simulations discussed above begin to address this gap. In notched tension tests, deformation concentrates at, and thus fracture initiates from, the specimen center due to the nonuniform gauge sections. Therefore, the strain at the specimen center at the moment of fracture in a notched tension

experiment can be taken to be the strain to fracture, $\bar{\varepsilon}^f$, of the material for that loading history. However, due to strain localization and the fact that fracture initiates at the through-thickness midplane, this strain cannot be measured experimentally. Therefore, here, the strains were extracted from the notched tension simulations at the point of experimentally observed displacement to final fracture.

It is known that the fracture strain of ductile metals is dependent on stress triaxiality, η, and Lode angle parameter, $\bar{\theta}$ [19,20]. Stress triaxiality, which is a measure of negative pressure of the stress state, is defined as:

$$\eta = \frac{\sigma_m}{\bar{\sigma}_{vM}} \qquad \text{Eq. 8}$$

where $\sigma_m = (\sigma_{11} + \sigma_{22} + \sigma_{33})/3$ is the hydrostatic stress. Lode angle parameter is defined as:

$$\bar{\theta} = 1 - \frac{2}{\pi}\arccos\left(\frac{3\sqrt{3}}{2}\frac{J_3}{\sqrt{J_2^3}}\right) \qquad \text{Eq. 9}$$

where $J_2 = \sqrt{\frac{1}{2}s_{ij}:s_{ij}}$ and $J_3 = \det(s_{ij})$ are the second and third invariants of the deviatoric stress tensor, respectively, with the deviatoric stress tensor, s_{ij}, being defined as $s_{ij} = \sigma_{ij} - \sigma_m\delta_{ij}$, where δ_{ij} is the Kronecker delta. The simulated Hill48 equivalent plastic strain at the center of each specimen versus stress triaxiality history is given for the notched tension tests in **Figure 10**. These results highlight the fact that during testing, the stress triaxiality at the specimens' center evolves. Therefore, an average stress triaxiality, η_{avg}, and an average Lode angle parameter, $\bar{\theta}_{avg}$, were calculated for each test as:

$$\eta_{avg} = \frac{1}{\bar{\varepsilon}^f} \int_0^{\bar{\varepsilon}^f} \eta \, d\bar{\varepsilon}^p_{Hill48}$$

$$\bar{\theta}_{avg} = \frac{1}{\bar{\varepsilon}^f} \int_0^{\bar{\varepsilon}^f} \bar{\theta} \, d\bar{\varepsilon}^p_{Hill48} \qquad \text{Eq. 10}$$

The η_{avg} and $\bar{\theta}_{avg}$ values and the fracture strain for each of the notched tension tests are summarized in **Table 4**. For the stress relieved samples and the stress states studied, the fracture strain along the BD was 30% higher on average compared to that along the PBD, which can be attributed to the elongated grain morphology. When the average stress triaxiality decreased from ~0.49 to ~0.39 and the average Lode angle parameter increased from ~0.51 to ~0.86, the fracture strain increased 33% along the BD and 47% along the PBD, thus, for the stress states studied, the fracture behavior of stress relieved L-PBF IN625 was found to depend more strongly on stress state along the PBD than the BD.

Along the PBD, the fracture strain for each stress state decreased by 45% on average after the stress relief heat treatment. This significant difference in fracture strain before and after stress relief heat treatment is largely due to the formation of the brittle δ phase. The formation of the δ phase also increased the stress state dependence of the fracture behavior, as the fracture strain of the as-built material increased by 36% when average stress triaxiality decreased from ~0.49 to ~0.40 and average Lode angle parameter increased from ~0.53 to ~0.84, while that of the stress relieved material increased by 47% for a similar level of stress state change. The fracture strains in the current study were investigated in the high stress triaxiality range ($\eta > 0.33$), in which damage accumulation is dominated by void nucleation, growth, and coalescence resulting in final fracture. Due to the higher strength and the sharp platelet morphology of the δ phase, its

presence in the microstructure will provide stress concentration sites, facilitating the process of void nucleation preceding growth and coalescence in the matrix, thus decreasing the strain to fracture. The drastic decrease in fracture strain after heat treatment highlights the importance of reducing the formation of δ phase in heat treated L-PBF IN625. In uniaxial tension along the PBD, the elongation to failure decreased by only 27% in the two conditions studied here, which significantly underestimates the influence of the δ phase on the fracture behavior of the material, emphasizing the insufficiency of using uniaxial tension only for estimating the influence of the δ phase on the fracture behavior of L-PBF IN625.

4. Conclusions

In this study, the microstructure, multiaxial plasticity behavior, and stress state dependent fracture behavior of both as-built and stress relieved L-PBF IN625 were investigated under tension dominated loading conditions. The influence of the δ phase on the fracture behavior of L-PBF IN625 was highlighted. The key findings of this study are as follows:

- The as-built L-PBF IN625 features a dendritic microstructure with elemental segregation between dendrites and interdendritic regions. After two hours of stress relief at 870 °C, approximately 10 vol. % δ phase formed.
- The stress relieved material exhibited anisotropic and stress state dependent plasticity behavior. A Hill48 plasticity model was able to capture the anisotropic and stress state plasticity behavior of both as-built and stress relieved L-PBF IN625.

- The fracture behavior of the stress relieved L-PBF IN625 was anisotropic, and on average, the fracture strain along the build direction was 30% higher than that of the perpendicular build direction for the stress states studied.
- While both materials in the as-built and stress relieved conditions showed stress state dependent fracture, the fracture behavior of the stress relieved material exhibited stronger stress state dependence along the build direction than along the perpendicular build direction.
- The formation of ~10 vol. % δ phase after stress relief resulted in a 9% increase in the ultimate tensile strength and a 45% decrease in the fracture strain. It also increased the stress state dependence of the fracture behavior so that for the same amount of increase in stress triaxiality and decrease in Lode angle parameter, the fracture strain increased by 36% for the as-built material but 47% for the stress relieved material.

Acknowledgments

This work was financially supported by the U. S. Department of Energy (DOE) via award no. DE-FE0031553 and the Office of Naval Research (ONR) via contract no. N00014-17-1-2567. The powder referred to as Carpenter powder was donated by Carpenter Technology, which is greatly appreciated by the authors.

Figures

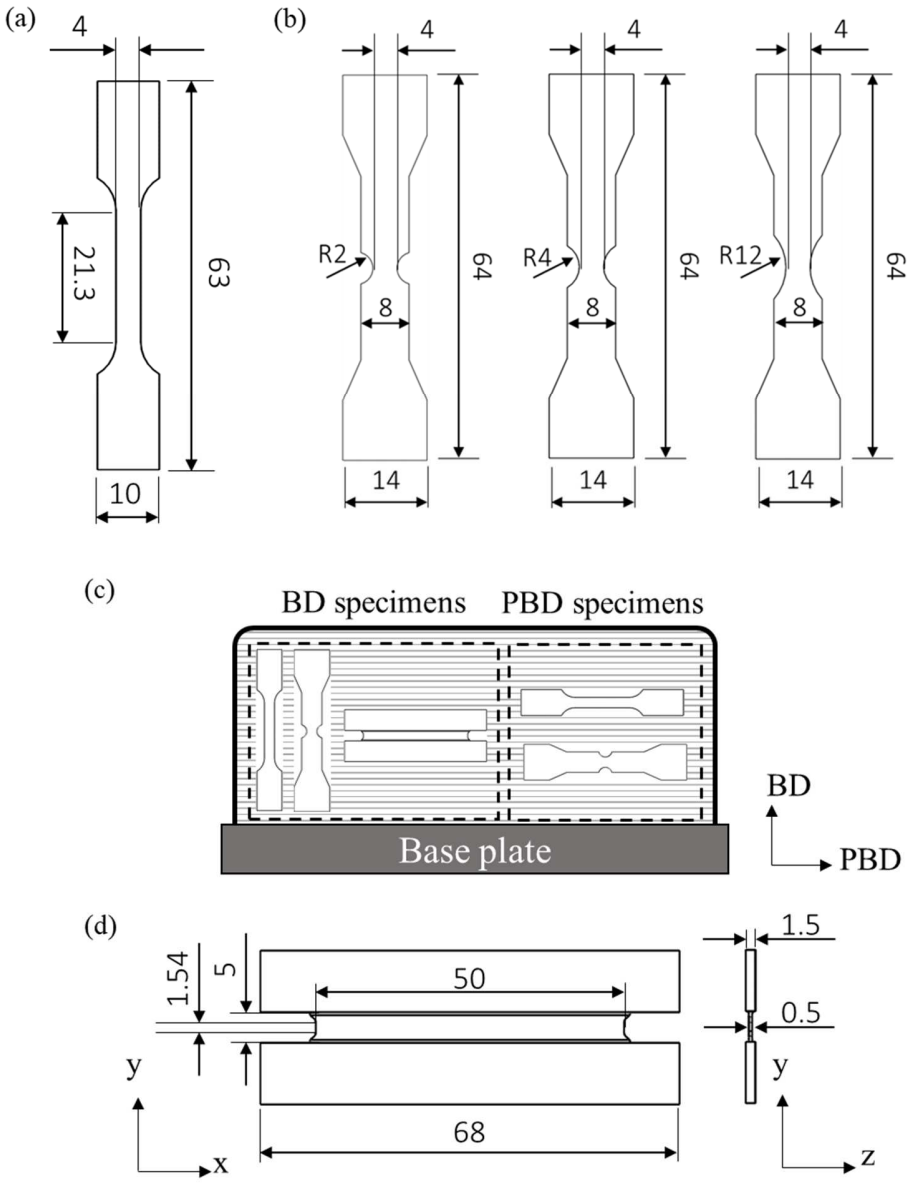

Figure 1: Geometry of (a) uniaxial tension, (b) notched tension, and (d) multiaxial plasticity specimens (dimensions in mm). The orientation of the specimens with respect to the build direction (BD) is shown in (c). The uniaxial tension and notched tension specimens had a thickness of 1.5 mm. The multiaxial plasticity specimen was adapted from [27].

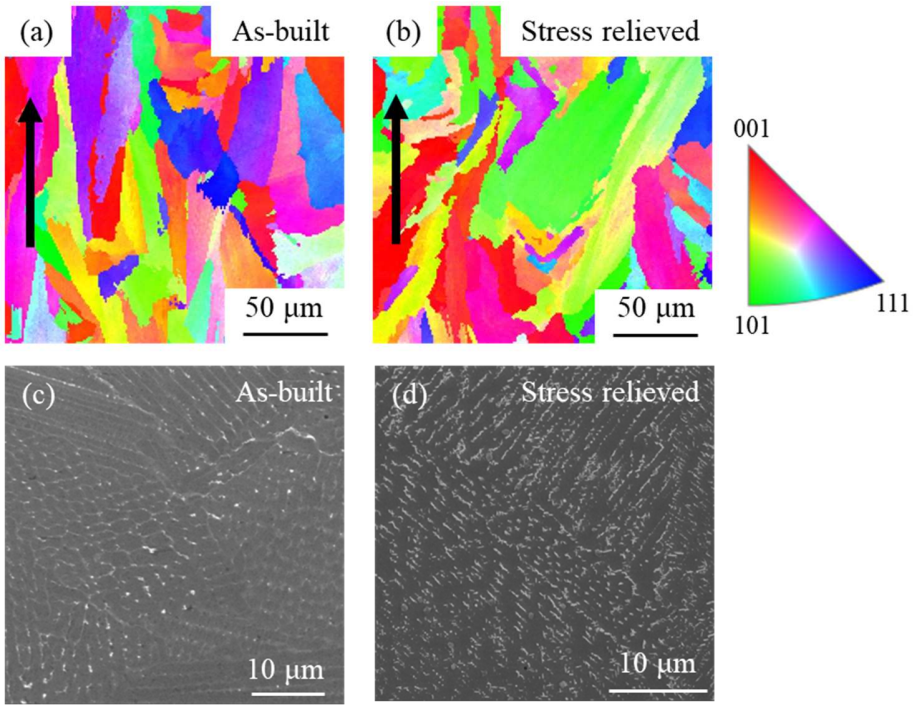

Figure 2: (a,b) EBSD and (c,d) SEM images of L-PBF IN625 in as-built (a, c) and stress relieved (b,c) conditions. The colors in (a,b) correspond to the *hkl* plane normals along the thickness direction (out of the page), and the arrows indicate the vertical build direction.

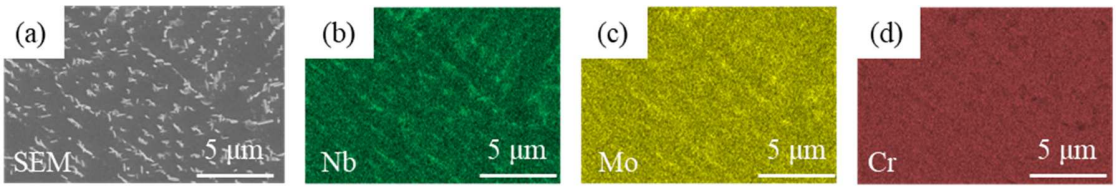

Figure 3: (a) SEM image of stress relieved L-PBF IN625 where bright regions correspond to the δ phase. (b-d) EDS elemental maps for the same region in (a) showing that the locations of the δ phase correspond to elevated concentrations of Nb and Mo and depletion of Cr.

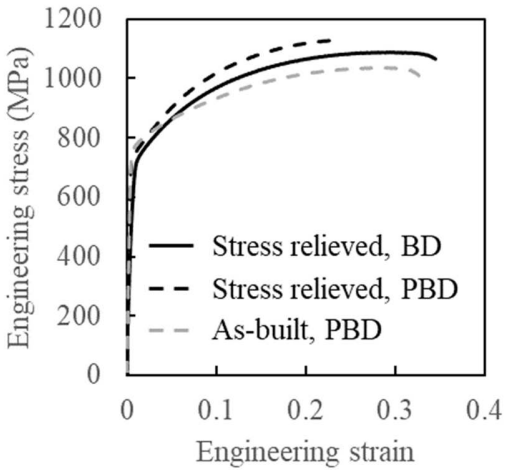

Figure 4: Engineering stress-strain curves for as-built and stress relieved L-PBF IN625 along the build direction (BD) and perpendicular build direction (PBD).

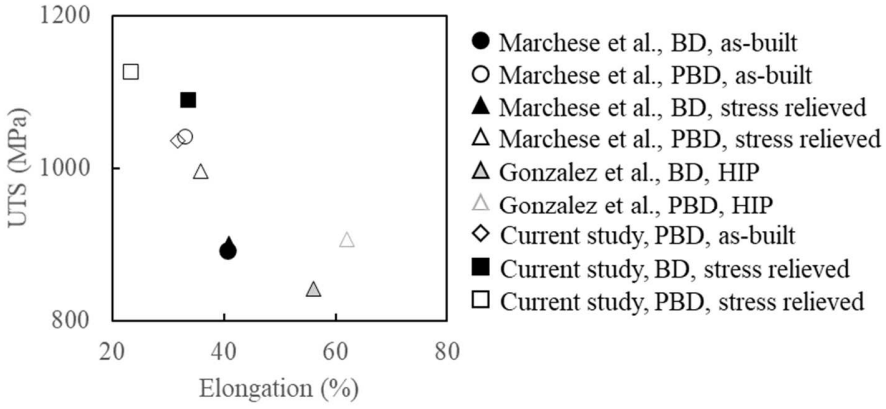

Figure 5: Ultimate tensile strength (UTS) versus elongation to failure for L-PBF IN625 subjected to different heat treatments from Marchese et al. [14], Gonzales et al. [4], and the current study.

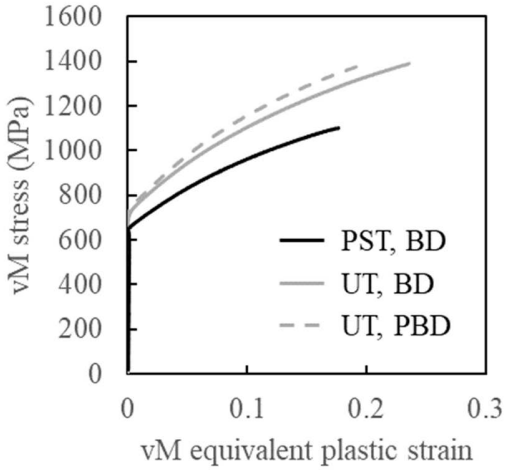

Figure 6: Strain hardening curves for stress relieved L-PBF IN625 under uniaxial tension (UT) in two directions and plane strain tension (PST) along the build direction.

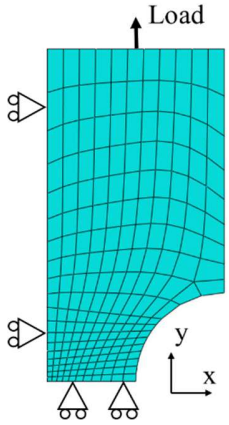

Figure 7: Illustration of boundary conditions applied and the mesh size that resulted in converging results. Note that symmetry boundary conditions were also applied along the *z* (thickness) direction.

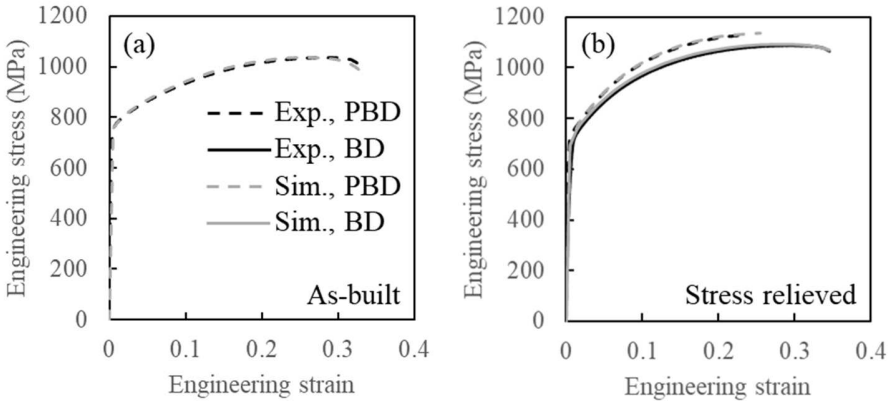

Figure 8: Comparison of engineering stress-strain curves obtained experimentally (black lines) and from finite element simulations using the Hill48 plasticity model (gray lines) for (a) as-built and (b) stress relieved L-PBF IN625. The legend in (a) applies to (b) as well.

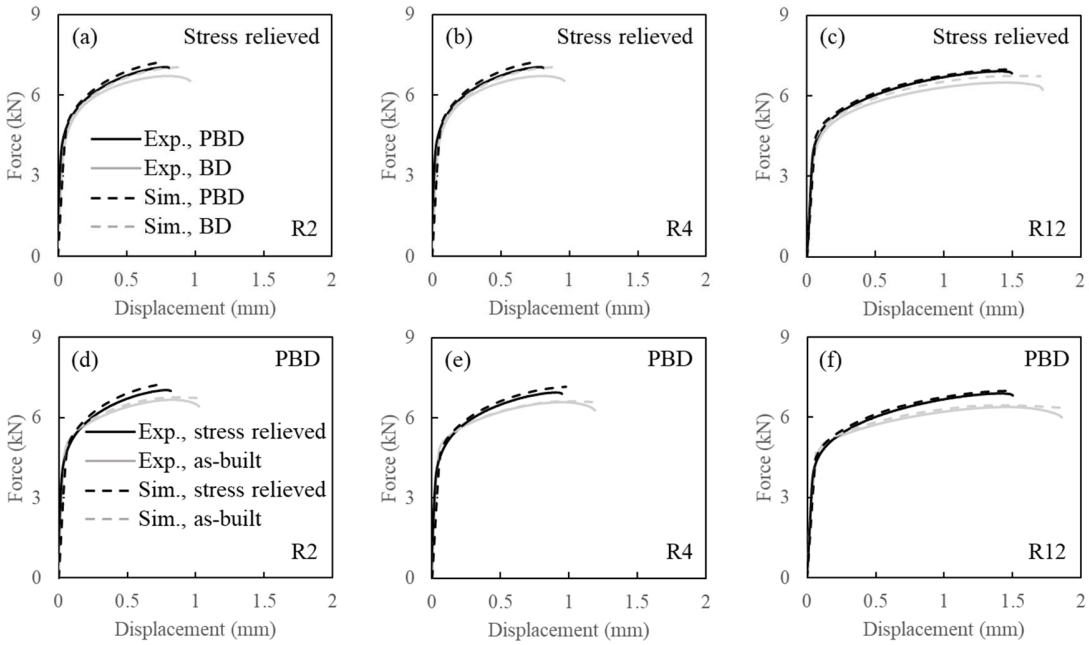

Figure 9: Force versus displacement behavior of notched tension samples obtained from experiments (solid lines) and finite element simulations (dashed lines). (a-c) Results for the stress relieved samples along two different orientations. (d-f) Results along the PBD for the as-built versus stress relieved samples. The legend in (a) applies to (a-c), and the legend in (d) applies to (d-f).

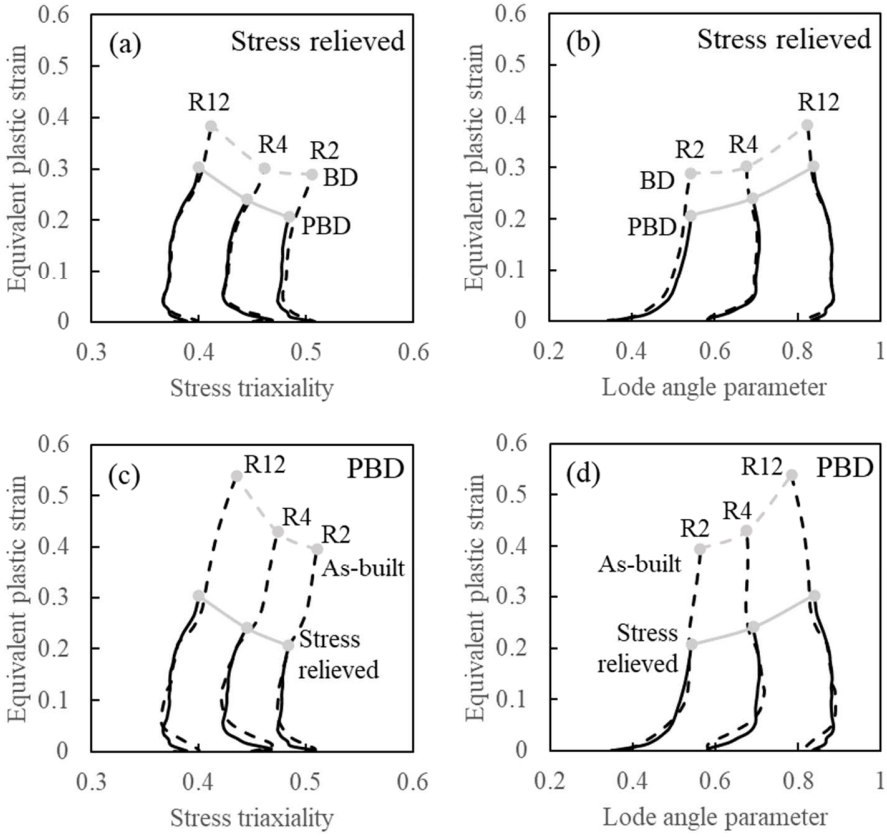

Figure 10: Evolution of Hill48 equivalent plastic strain versus stress triaxiality and Lode angle parameter in notched tension tests, where the symbols represent final failure. (a,b) Comparison of behavior in two directions in the stress relieved condition, and (c,d) comparison of as-built versus stress relieved results in the perpendicular build direction.

Tables

Table 1: Elemental composition (wt.%) of the IN625 walls in the as-built and stress relieved states.

	C	Mn	Si	Cr	Fe	Mo	Ti	Al	Nb	Ta
As-built walls (Carpenter powder)	0.018 ±0.001	0.33± 0.01	0.33± 0.01	21.9 ±0.4	4.69± 0.09	8.29 ±0.2	0.036± 0.002	0.026± 0.002	3.42± 0.07	<0.002
Stress relieved walls (3D Systems powder)	0.017 ±0.001	0.28± 0.01	0.28± 0.01	21.1 ±0.4	3.36± 0.07	8.48 ±0.2	0.047± 0.002	0.045± 0.002	3.92± 0.08	<0.002

Table 2: Tensile properties of IN625 manufactured by different techniques and with different heat treatments.

Source	Year	Manufacturing method	Heat treatment	δ phase percent	Tensile direction	UTS (MPa)	Elongation (%)
ASTM (F3056) [38]		PBF				> 485	> 30
ASTM (B443) [39]		Wrought				> 690	> 30
EOS [40]	2017	L-PBF	As-built	Not reported	BD	870	48
					PBD	980	33
			870 °C for 1 hr		BD	890	49
					PBD	1000	34
Marchese et al. [14]	2020	L-PBF	As-built	0	BD	891	40.7
				0	PBD	1041	33.1
			870 °C for 1 hr	Present but not quantified	BD	900	40.9
				Present but not quantified	PBD	996	35.8
Gonzalez et al. [4]	2019	L-PBF	HIP (1163 °C and 102 MPa for 3 hrs)	Not reported	BD	842	56
					PBD	906	62
		Electron beam-PBF			BD	723	27
					PBD	849	44
		Binder Jetting			BD	708	27
					PBD	707	59
Xu et al. [30]	2013	Pulsed plasma arc deposition	980 °C for 1 hr and 720 °C for 8 hrs, then 620 °C for 8 hrs	Present but not quantified	PBD	851	44
Wang et al. [31]	2016	L-PBF	As-built	0	PBD	878.5	30
Mu et al. [17]	2018	Cast	1200 ° C for 1 hr + 750 °C for up to 17000 hrs	0	N/A	380 - 425	50 - 65
				17		650 - 730	17 - 25
				40		800 - 825	9 - 10
			800 °C for 6 hrs	1.38		1236	21
			1050 ° C for 5 - 10 min + 800 °C for 6 hrs	0.67		1209	22
				0.68		1208	21

Table 3: Hill48 plasticity model parameter values.

	P_{11}	P_{12}	P_{33}*	A	ε_0	n	K
As-built	0.94	-0.33	3	2110 MPa	0.082	0.41	1264 MPa
Stress relieved				2172 MPa	0.038	0.34	1417 MPa

* Due to lack of experimental data under shear, this value was assumed.

Table 4: Fracture strains of L-PBF IN625 in as-built and stress relieved conditions.

	R2			**R4**			**R12**		
	η_{avg}	$\bar{\theta}_{avg}$	$\bar{\varepsilon}^f$	η_{avg}	$\bar{\theta}_{avg}$	$\bar{\varepsilon}^f$	η_{avg}	$\bar{\theta}_{avg}$	$\bar{\varepsilon}^f$
As-built, PBD	0.49	0.53	0.40	0.45	0.68	0.43	0.40	0.84	0.54
Stress relieved, PBD	0.48	0.51	0.21	0.43	0.69	0.24	0.38	0.87	0.30
Stress relieved, BD	0.49	0.51	0.29	0.44	0.69	0.30	0.39	0.86	0.38

References

[1] L. M. Suave, J. Cormier, P. Villechaise, A. Soula, Z. Hervier, D. Bertheau, and J. Laigo, "Microstructural evolutions during thermal aging of alloy 625: Impact of temperature and forming process," *Metall. Mater. Trans. A*, vol. 45, no. 7, pp. 2963–2982, 2014.

[2] E. A. Lass, M. R. Stoudt, M. E. Williams, M. B. Katz, L. E. Levine, T. Q. Phan, T. H. Gnaeupel-Herold, and D. S. Ng, "Formation of the Ni3Nb δ-Phase in Stress-Relieved Inconel 625 Produced via Laser Powder-Bed Fusion Additive Manufacturing," *Metall. Mater. Trans. A*, vol. 48, no. 11, pp. 5547–5558, 2017.

[3] G. Marchese, M. Lorusso, S. Parizia, E. Bassini, J. W. Lee, F. Calignano, D. Manfredi, M. Terner, H. U. Hong, D. Ugues, M. Lombardi, and S. Biamino, "Influence of heat treatments on microstructure evolution and mechanical properties of Inconel 625 processed by laser powder bed fusion," *Mater. Sci. Eng. A*, vol. 729, no. May, pp. 64–75, 2018.

[4] J. A. Gonzalez, J. Mireles, S. W. Stafford, M. A. Perez, C. A. Terrazas, and R. B. Wicker, "Characterization of Inconel 625 fabricated using powder-bed-based additive manufacturing technologies," *J. Mater. Process. Technol.*, vol. 264, no. August 2017, pp. 200–210, 2019.

[5] A. Kreitcberg, V. Brailovski, and S. Turenne, "Effect of heat treatment and hot isostatic pressing on the microstructure and mechanical properties of Inconel 625 alloy processed by laser powder bed fusion," *Mater. Sci. Eng. A*, vol. 689, no. February, pp. 1–10, 2017.

[6] T. DebRoy, H. L. Wei, J. S. Zuback, T. Mukherjee, J. W. Elmer, J. O. Milewski, A. M. Beese, A. Wilson-Heid, A. De, and W. Zhang, "Additive manufacturing of metallic

components – Process, structure and properties," *Prog. Mater. Sci.*, vol. 92, pp. 112–224, 2018.

[7] H. Chandler, *Heat treater's guide: practices and procedures for nonferrous alloys*. ASM international, 1996.

[8] F. Zhang, L. E. Levine, A. J. Allen, M. R. Stoudt, G. Lindwall, E. A. Lass, M. E. Williams, Y. Idell, and C. E. Campbell, "Effect of heat treatment on the microstructural evolution of a nickel-based superalloy additive-manufactured by laser powder bed fusion," *Acta Mater.*, vol. 152, pp. 200–214, 2018.

[9] L. Mataveli Suave, J. Cormier, D. Bertheau, P. Villechaise, A. Soula, Z. Hervier, and F. Hamon, "High temperature low cycle fatigue properties of alloy 625," *Mater. Sci. Eng. A*, vol. 650, pp. 161–170, 2016.

[10] V. Shankar, K. Bhanu Sankara Rao, and S. L. Mannan, "Microstructure and mechanical properties of Inconel 625 superalloy," *J. Nucl. Mater.*, vol. 288, no. 2–3, pp. 222–232, 2001.

[11] J. Mittra, S. Banerjee, R. Tewari, and G. K. Dey, "Fracture behavior of Alloy 625 with different precipitate microstructures," *Mater. Sci. Eng. A*, vol. 574, pp. 86–93, 2013.

[12] G. Lindwall, C. E. Campbell, E. A. Lass, F. Zhang, M. R. Stoudt, A. J. Allen, and L. E. Levine, "Simulation of TTT Curves for Additively Manufactured Inconel 625," *Metall. Mater. Trans. A*, vol. 50, no. 1, pp. 457–467, 2019.

[13] K. Inaekyan, A. Kreitcberg, S. Turenne, and V. Brailovski, "Microstructure and mechanical properties of laser powder bed-fused IN625 alloy," *Mater. Sci. Eng. A*, vol. 768, no. July, p. 138481, 2019.

[14] G. Marchese, S. Parizia, M. Rashidi, A. Saboori, D. Manfredi, D. Ugues, M. Lombardi, E. Hryha, and S. Biamino, "The role of texturing and microstructure evolution on the tensile behavior of heat-treated Inconel 625 produced via laser powder bed fusion," *Mater. Sci. Eng. A*, vol. 769, no. July 2019, 2020.

[15] M. R. Stoudt, E. A. Lass, D. S. Ng, M. E. Williams, F. Zhang, C. E. Campbell, G. Lindwall, and L. E. Levine, "The Influence of Annealing Temperature and Time on the Formation of δ-Phase in Additively-Manufactured Inconel 625," *Metall. Mater. Trans. A*, vol. 49, no. 7, pp. 3028–3037, 2018.

[16] S. Floreen, G. E. Fuchs, W. J. Yang, and E. A. Loria, "Superalloys 718, 625, 706 and various derivatives," in *3rd Proc. Int. Symp*, 1994, pp. 13–37.

[17] Y. Q. Mu, C. S. Wang, W. L. Zhou, and L. Z. Zhou, "Tensile Properties of Cast Alloy IN625 in Relation to δ Phase Precipitation," *Acta Metall. Sin. (English Lett.*, vol. 32, no. 4, pp. 535–540, 2019.

[18] Y. Bai and T. Wierzbicki, "A new model of metal plasticity and fracture with pressure and Lode dependence," *Int. J. Plast.*, vol. 24, no. 6, pp. 1071–1096, 2008.

[19] Y. Bai and T. Wierzbicki, "Application of extended Mohr-Coulomb criterion to ductile fracture," *Int. J. Fract.*, vol. 161, no. 1, pp. 1–20, 2010.

[20] Y. Bao and T. Wierzbicki, "On the cut-off value of negative triaxiality for fracture," *Eng. Fract. Mech.*, vol. 72, no. 7, pp. 1049–1069, 2005.

[21] A. E. Wilson-Heid, S. Qin, and A. M. Beese, "Anisotropic multiaxial plasticity model for laser powder bed fusion additively manufactured Ti-6Al-4V," *Mater. Sci. Eng. A*, vol. 738, no. September, pp. 90–97, 2018.

[22] A. E. Wilson-Heid and A. M. Beese, “Fracture of laser powder bed fusion additively manufactured Ti–6Al–4V under multiaxial loading: Calibration and comparison of fracture models,” *Mater. Sci. Eng. A*, no. April, p. 137967, 2019.

[23] M. B. Gorji, T. Tancogne-Dejean, and D. Mohr, “Heterogeneous random medium plasticity and fracture model of additively-manufactured Ti-6Al-4V,” *Acta Mater.*, 2018.

[24] T. Tancogne-Dejean, C. C. Roth, U. Woy, and D. Mohr, “Probabilistic fracture of Ti-6Al-4V made through additive layer manufacturing,” *Int. J. Plast.*, vol. 78, pp. 145–172, 2016.

[25] A. E. Wilson-Heid, S. Qin, and A. M. Beese, “Multiaxial Plasticity and Fracture Behavior of Stainless Steel 316L by Laser Powder Bed Fusion: Experiments and Computational Modeling,” *Acta Mater.*, vol. 199, pp. 578–592, 2020.

[26] ASTM E8/E8M, “Standard test methods for tension testing of metallic materials,” *ASTM International*, 2010. .

[27] D. Mohr and M. Oswald, “A new experimental technique for the multi-axial testing of advanced high strength steel sheets,” *Exp. Mech.*, vol. 48, no. 1, pp. 65–77, 2008.

[28] S. Qin, R. McLendon, V. Oancea, and A. M. Beese, “Micromechanics of multiaxial plasticity of DP600: experiments and microstructural deformation modeling,” *Mater. Sci. Eng. A*, vol. 721, pp. 168–178, Feb. 2018.

[29] A. Kreitcberg, V. Brailovski, and S. Turenne, “Elevated temperature mechanical behavior of IN625 alloy processed by laser powder-bed fusion,” *Mater. Sci. Eng. A*, vol. 700, no. June, pp. 540–553, 2017.

[30] F. Xu, Y. Lv, Y. Liu, B. Xu, and P. He, “Effect of heat treatment on microstructure and mechanical properties of inconel 625 alloy fabricated by pulsed plasma arc deposition,”

Phys. Procedia, vol. 50, no. October 2012, pp. 48–54, 2013.

[31] P. Wang, B. Zhang, C. C. Tan, S. Raghavan, Y. F. Lim, C. N. Sun, J. Wei, and D. Chi, "Microstructural characteristics and mechanical properties of carbon nanotube reinforced Inconel 625 parts fabricated by selective laser melting," *Mater. Des.*, vol. 112, pp. 290–299, 2016.

[32] R. v. Mises, "Mechanik der festen Körper im plastisch-deformablen Zustand," *Nachrichten von der Gesellschaft der Wissenschaften zu Göttingen, Mathematisch-Physikalische Klasse*, pp. 582–592, 1913.

[33] R. Hill, "A theory of the yielding and plastic flow of anisotropic metals," in *In Proceedings of the Royal Society of London A: Mathematical, Physical and Engineering Sciences*, 1948, pp. 281–297.

[34] M. B. Gorji and D. Mohr, "Micro-tension and micro-shear experiments to characterize stress-state dependent ductile fracture," *Acta Mater.*, vol. 131, pp. 65–76, 2017.

[35] C. C. Roth and D. Mohr, "Ductile fracture experiments with locally proportional loading histories," *Int. J. Plast.*, vol. 79, pp. 328–354, 2016.

[36] J. Ha, M. Baral, and Y. P. Korkolis, "Plastic anisotropy and ductile fracture of bake-hardened AA6013 aluminum sheet," *Int. J. Solids Struct.*, vol. 155, pp. 123–139, 2018.

[37] "Abaqus User Manual v2017," *DS SIMULIA*, 2017.

[38] ASTM F3056-14, "Standard Specification for Additive Manufacturing Nickel Alloy (UNS N06625) with Powder Bed Fusion," *ASTM Int.*, 2014.

[39] ASTM B443 - 19, "Standard Specification for Nickel-Chromium-Molybdenum-Columbium Alloy and Nickel-Chromium-Molybdenum-Silicon Alloy Plate, Sheet, and

Strip," *ASTM Int.*, 2019.

[40] EOS GmbH, "Nickel Alloy IN625 Data Sheet," vol. 49, no. 0, pp. 1–6, 2017.